Published in final edited form as:
Science. 2010 August 13; 329(5993): 830–834. doi:10.1126/science.1192033.

Three-dimensional, Flexible Nanoscale Field Effect Transistors as Localized Bioprobes

Bozhi Tian[1,*], **Tzahi Cohen-Karni**[2,*], **Quan Qing**[1], **Xiaojie Duan**[1], **Ping Xie**[1], and **Charles M. Lieber**[1,2,†]

[1]Department of Chemistry and Chemical Biology, Harvard University, Cambridge, Massachusetts, 02138, USA.

[2]School of Engineering and Applied Sciences, Harvard University, Cambridge, Massachusetts, 02138, USA.

Abstract

Nanoelectronic devices offer substantial potential for interrogating biological systems, although nearly all work has focused on planar device designs. We have overcome this limitation through synthetic integration of a nanoscale field effect transistor (nanoFET) device at the tip of an acute-angle kinked silicon nanowire, where nanoscale connections are made by the arms of the kinked nanostructure and remote multilayer interconnects allow three-dimensional (3D) probe presentation. The acute-angle probe geometry was designed and synthesized by controlling *cis* versus *trans* crystal conformations between adjacent kinks, and the nanoFET was localized through modulation doping. 3D nanoFET probes exhibited conductance and sensitivity in aqueous solution independent of large mechanical deflections, and demonstrated high pH sensitivity. Additionally, 3D nanoprobes modified with phospholipid bilayers can enter single cells to allow robust recording of intracellular potentials.

Nanowire and nanotube electrical devices have been exploited for ultrasensitive detection of biological markers (1) and high-resolution extracellular recording from cells (2–5). However, localized and tunable 3D sensing and recording using the prototypical nanoelectronic device, a nanoscale field-effect transistor (nanoFET) (6), have not been demonstrated because almost all examples of these devices are created on planar substrates. Ideally, rather than force the cell to conform to the substrate, a movable nanoFET with the necessary source (S) and drain (D) electrical connections could move into contact with the cell and probe within the cell membrane. However, minimally-invasive insertion of a nanoFET into the confined 3D space of single cells or even 3D cellular networks is a significant challenge because the S and D typically dominate the overall device size and define a planar and rigid structure regardless of whether the nanoFET is on or suspended above a substrate (5,6).

Existing probes capable of intracellular sensing and recording include voltage-sensitive optical dyes (7,8) and single-terminal glass (9–11) or carbon (12–14) microelectrodes. Voltage sensitive dyes can be readily used to interrogate action potentials with high spatial resolution, but also have limitations in terms of signal-to-noise ratio, pharmacological side

†To whom correspondence should be addressed. cml@cmliris.harvard.edu.
*These authors contributed equally to this work.

Supporting Online Material
www.sciencemag.org
Materials and Methods
Figs. S1–S5

effects, phototoxicity, and difficulty in differentiating single spikes (7,8). For electrical probes, the single electrical connection facilitates design and mechanical insertion into cells, but the requirement of direct ionic and/or electrical junctions between probe tips and cytosol also introduce several limitations. First, the tip size of these probes (0.2 ~ 5 μm) (9–14) is a compromise between being small enough to penetrate or rupture the cell membrane with minimum damage (< 5 μm), but large enough to yield a sufficiently low enough junction impedance (13,15) (> 0.2 μm) so that small cellular signals can be discerned from thermal noise. Second, direct exposure of intracellular species to extraneous probe surfaces or electrolytes in probe lumen (9–13) especially for larger glass micropipettes might induce irreversible changes to cells, and thus prevent long-term and non-invasive cellular recordings. Finally, these probe techniques are intrinsically passive, and are not capable of built-in signal processing and facile integration with other circuitries especially given the emerging need to enabling a cell-machine communication (15).

FETs can function in a sub-10 nm size regime (16). NanoFETs could function as mechanically non-invasive probes capable of entering cells through endocytic pathways as can occur with nanoparticles (17). Moreover, when interfacing with cells, the FETs process input/output information without the need for direct exchange with cellular ions, thus interfacial impedance and biochemical invasiveness to cells can be minimized. In addition, because signals are transduced by change in field/potential at well-isolated surfaces, FETs can detect cellular potential (2–5) as well as biological macromolecules (1), and could be integrated for potential multiplexed intracellular measurements. Unfortunately and as discussed above, the requirement of two electrical contacts to a FET, the S and D, makes design of 3D probes and their minimally-invasive insertion into a cell or tissue a substantial challenge.

Recently, we demonstrated that variation of reactant pressure during silicon nanowire (SiNW) growth could introduce reproducible 120° kinks (18), and that the junction regions could be doped to create p-n diodes and FETs. We used this methodology to create a two-terminal FET probe that could be inserted into single cells. The growth of kinked SiNWs had to be tailored in the following ways. First, we needed to incorporate two or three *cis*-linked kinked units to yield probe tip angles of 60° or 0°, respectively (Fig. 1A, top and middle). Because two *trans*-linked units (Fig. 1A, bottom) would yield an unusable probe tip, the selective synthesis of *cis*-linked units is central to our probe geometry design. A representative scanning electron microscopy (SEM) image of an 80 nm diameter, doubly-kinked SiNW with an intervening segment length (*L*) of ~160 nm between kink units (Fig. 1B) shows well-defined *cis*-linkage and an overall 60° tip angle (Fig. 1A, top). To investigate our ability to synthesize this *cis*-linkage of kink structural units reproducibly, we analyzed their fraction as a function of *L* in doubly kinked SiNWs. Notably, the plot of *cis*/(*cis* + *trans*) as *L* was varied from ~700 to 50 nm (Fig. 1C) shows that the '*cis*' conformation becomes dominant as *L* decreases. We can selectively synthesize *cis*-linked kinked units in good yield [Fig. S1A (19)], *e.g.* ~ 66 % where *L* ~ 50 nm, and such conformation control is also maintained in the growth of complex probe structures [Fig. S1B (19)].

The second design consideration made use of selective in-situ doping during synthesis to localize and self-label the nanoscale FET element adjacent to the topologically defined probe tip (Fig. 1A, magenta segments), and simultaneously "wire-up" the FET channel with nanowire S/D components (Fig. 1A, blue segments). Similar to studies of single-kinked nanowires (18) we use heavy n^{++}-type doping for the nanowire S/D arms, and reduce the concentration to light n-type doping to introduce a short ~200 nm region immediately following the growth of two sequential kinks and serving as the 'point-like' FET detector of

the overall probe. Scanning gate microscopy (SGM) measurements [Fig. S1 (19)] showed that nanoscale FETs were integrated at the probe tip during overall synthesis.

We have also examined the size limits of these synthetic bioprobes in terms of the overall nanowire diameter and length *L* between kinks and find that well-defined probe structures are possible for values as small as ~ 18 and 15 nm, respectively (Fig. 1D, Fig. S2) (19). These data show that it is possible to create active semiconductor probes with dimensions smaller than microtubules in cells (20).

We next designed an unconventional nanoelectronic device fabrication approach that would allow these probes to be used as cellular probes. Remote electrical interconnects were made to the S/D nanowire arms on ultrathin SU-8 polymer ribbons above a sacrificial layer (Fig. 2A, upper panel). The interfacial stress between materials (21) was used to bend the probe upward after a final lift-off process (Fig. 2A, lower panel); see Fig. S3A for fabrication details (19). Our nanoprobes are distinct from previous nanoelectronic devices because, (i) the FET channel (Fig. 2A, white dots) and S/D (Fig. 2A, black segments) components are integrated epitaxially at the nanoscale through synthesis (Fig. 1) similar to single-kink structures (17), (ii) the nanoscale FET is free-standing and (iii) the acute-angle kinked nanowire geometry and the extended S/D arms spatially separate the functional nanoscale FET from the bulky interconnects by a distance up to ~ 30 μm, comparable to the size of single cells, so that the nanoscale interrogation can be realized with minimum interference from macroscopic interconnects.

A representative SEM image of one free-standing device (Fig. 2B, I) demonstrates that the 60° kinked probe is intact after fabrication with the two nanowire arm terminals sandwiched between SU-8 polymer and metal contacts. We achieved ≥90% yields with ~30 nanoprobe devices per chip. In addition, the probe height and angle (*H* and, Fig. 2A) were systematically tuned by changing the length and thickness of the free-standing part of the metal interconnects/SU-8 backbone (Fig. S3B) (19). We also find that the nanoprobe *H* and θ typically increase when submerged in aqueous solution, *e.g.* *H*/θ of the device (Fig. 2B, I) are 25 μm/43° and 38 μm/90° in air and water, respectively (Fig. 2B, II and III). This change is reversible and suggests that the nanoprobe devices are intrinsically flexible, and moreover, that the specific orientation could be manipulated chemically (21). Last, free-standing 3D FET devices have been stored in air for at least 8 months without appreciable changes in nanoprobe orientations and FET sensitivity (less than 7 and 3%, respectively).

The sensitivity of the 3D nanoscale FET probes was characterized in phosphate buffered saline (PBS) solution (Fig. 2C, and Fig. S4A). Measurements of the conductance vs. reference potential for the 3D probes yielded sensitivities of 4–8 μS/V. Similar sensitivities, 4–8 μS/V, were observed for kinked nanowire devices fabricated on planar substrates, thus indicating that there is no degradation in the bent 3D configuration. We note that the sensitivity contribution from the lightly-doped nanoFET is > 97% of the total device response. Localized detection by the lightly-doped region versus the heavily-doped S/D nanowire arms is consistent with our SGM measurements on these acute-angle probes (Fig. S1) and previous studies of single-kinked nanowires (17).

To further highlight the flexibility and robustness of the 3D nanoFET probes we have characterized the conductance and sensitivity in PBS as a glass micropipette was used to vary the tip height (inset, Fig. 2C). Typical data (Fig. 2C) yield a <20 nS conductance change for a ca. ±10 μm change in *H*, which corresponds to < 0.31 % fluctuation in the total device conductance. Likewise, the device sensitivity remains stable with a maximum change of ~0.15 μS/V or 2.4 % variation for this ca. ± 10 μm tip height change. In addition, repetitive bending does not degrade the FET performance in these nanowire probes. Finally,

the stable FET performance in different bending configurations suggests the capability of reliable sensing and recording in a flexible and tunable 3D manner from single devices, which could be particularly beneficial for interfacing with soft and motile biological systems.

We tested the sensing capabilities of the 3D SiNW probes by recording the response to variations in solution pH within a poly-dimethylsiloxane (PDMS) microfluidic channel (Fig. 2D, inset). Stepwise potential increases from 7.5 to 6.7 by 0.1 pH units were readily resolved, and the sensitivity of ~ 58 mV/pH was near the Nernstian limit. Indeed, high-resolution recording indicates the capability of resolving changes as small as 0.02 pH units [Fig. S4B(19)] in this physiologically-relevant range of pH.

In order to use the 3D nanoFET probes in cells (Fig. 3A), we coated them with phospholipid bilayers, which can form on a variety of nanostructured inorganic materials (22–24) and also fuse with cell membranes (24). Accordingly, we modified the negatively charged SiO_2 surface of the SiNWs by fusion with unilamellar vesicles of phospholipid bilayers (1,2-dimyristoyl-sn-glycero-3-phosphocholine (DMPC)) (19,22). Fluorescence microscopy images of dye-labeled DMPC modified probes (Fig. 3B) indicate that the lipid bilayers form a continuous shell on our acute-angle nanoprobes, and device measurements show that the lipid surface coating results in < 1% changes in both the nanoFET conductance and sensitivity. We then monitored the calibrated potential change of phospholipid-modified nanoFET probe while an isolated HL-1 cell (25) was moved into contact and then away from the nanoprobe using a glass micropipette under microscopy visualization (top, Fig. 3C).The micropipette was also used to clamp the intracellular potential at −50 mV (11). Notably, measurement of the potential versus time from the nanoFET probe shows a sharp ~52 mV drop within 250 ms after cell/tip contact. While the nanoprobe tip is within the cell, the recorded potential maintains a relatively constant value of ca. −46 mV, and then returns to baseline when the cell was detached from the nanowire probe end. Interestingly, nanoFET probes of similar sensitivity that were not coated with a phospholipid bilayer modification exhibited only baseline fluctuations (< ±1 mV), as the HL-1 cell was brought into contact and then retracted (Fig. 3D). These results suggest the biochemical state of the nanowire probe surfaces (26) is critical for assisting access to the intracellular region, possibly through membrane fusion [Fig. 3A (24)], and is distinct from larger, more rigid probes commonly used for intracellular electrical recording.

We have also investigated the formation of intracellular interfaces between our 3D nanoFET probes and spontaneously firing electrogenic cells. Embryonic chicken cardiomyocytes were cultured on polydimethylsiloxane (PDMS) substrates (2) and then positioned to place individual cells over phospholipid bilayer-modified vertical ($\theta = 90°$) nanoprobes within a cell perfusion chamber (2,4) as shown schematically in Fig. 4A. Representative conductance versus time data recorded from a 3D nanoFET probe initially in gentle contact with a spontaneously beating cardiomyocyte cell (Fig. S5A) (19) showed a sequence of distinct features (Fig. 4B). Initially, we observe regularly spaced spikes with a frequency of ca. 2.3 Hz consistent with beating cardiomyocyte (Fig. 4B, I). The peaks have a potential change of ~ 3–5 mV, a signal-to-noise (S/N) ≥2 and a sub-millisecond width (Fig. 4C, I). The peak amplitude, shape and width are similar to extracellular recordings made with nanowire devices on substrates (2), and moreover, optical images recorded at the same time [Fig. S5A (19)] are consistent with extracellular signals.

After a relatively brief (~40 s) period of extracellular signals, we observed several pronounced changes in recorded signals (Figs. 4B and C, II and III) without application of external force to the PDMS/cell support. Specifically, the initial extracellular signals gradually disappeared (Figs. 4B and C, II, magenta stars). There was a concomitant decrease

in baseline potential and new peaks emerged that had an opposite sign, similar frequency, much greater amplitude, and longer duration (Fig. 4B, II, green stars). These new peaks, which are coincident with cell beating, rapidly reached a steady state (Fig. 4B, III) with an average calibrated peak amplitude of ~ 80 mV and duration of ~ 200 ms. The amplitude, sign, and duration are near those reported for whole-cell patch clamp recordings from cardiomyocytes (27,28), and thus we conclude that these data represent a transition to steady-state intracellular recording (Fig. 4A, right) with the 3D nanowire probe.

Detailed analysis of the latter steady-state peaks (Fig. 4C, III) shows five characteristic phases of a cardiac intracellular potential (27,28), including (a) resting state, (b) rapid depolarization, (c) plateau, (d) rapid repolarization and (e) hyperpolarization. In addition, a sharp transient peak (blue star) and the notch (orange star) possibly associated with the inward sodium and outward potassium currents (28) can be resolved. Optical images recorded at the same time as these intracellular peaks (Fig. S5B) showed the kinked nanowire probe tips in a possible intracellular region of the cell (19). When the PDMS/cell substrate was mechanically-retracted from the 3D kinked nanowire devices, the intracellular peaks disappeared, but reappeared when the cell substrate was brought back into gentle contact with the device. This process could be repeated multiple times without degradation in the recorded signal. We note that when vertical 3D nanoprobe devices were bent into a configuration with angle $\theta < \sim 50^\circ$ with respect to the substrate, or when kinked nanowire devices were fabricated on planar substrates, we could record only extracellular signals. These results confirm that electrical recording arises from the highly-localized, point-like nanoFET near the probe tip, which (a) initially records only extracellular potential, (b) simultaneously records both extracellular and intracellular signals as the nanoFET spans the cell membrane, and (c) records only intracellular signals when fully inside the cell.

Additional work remains in order to develop this new synthetic nanoprobe as routine tool like the patch-clamp micropipette (10,11), although we believe that there are already clear advantages: Electrical recording with kinked nanowire probes is relatively simple without the need for resistance or capacitance compensation (9,11), the nanoprobes are chemically less invasive than pipettes as there is no solution exchange, the small size and biomimetic coating minimizes mechanical invasiveness, and the nanoFETs have high spatial and temporal resolution for recording.

Supplementary Material

Refer to Web version on PubMed Central for supplementary material.

Acknowledgments

We thank Prof. G. Yellen, Prof. W. C. Claycomb, Prof. B. P. Bean, Prof. P. T. Ellinor, Dr. G. H. Yu, Dr. D. Casanova, Dr. B. P. Timko and Dr. T. Dvir for help with experiments and data analysis. C.M.L. acknowledges support from a National Institutes of Health Director's Pioneer Award and a McKnight Foundation Neuroscience.

References and Notes

1. Giljohann DA, Mirkin CA. Drivers of biodiagnostic development. Nature. 2009; 462:461–464. [PubMed: 19940916]
2. Cohen-Karni T, Timko BP, Weiss LE, Lieber CM. Flexible electrical recording from cells using nanowire transistor arrays. Proc. Natl. Acad. Sci. USA. 2009; 106:7309–7313. [PubMed: 19365078]
3. Eschermann JF, Stockmann R, Hueske M, Vu XT, Ingebrandt S, Offenhausser A. Action potentials of HL-1 cells recorded with silicon nanowire transistors. Appl. Phys. Lett. 2009; 95:083703.

4. Qing Q, Pal SK, Tian BZ, Duan XJ, Timko BP, Cohen-Karni T, Murthy VN, Lieber CM. Nanowire transistor arrays for mapping neural circuits in acute brain slices. Proc. Natl. Acad. Sci. USA. 2010; 107:1882–1887. [PubMed: 20133836]
5. Heller I, Smaal WTT, Lemay SG, Dekker C. Probing macrophage activity with carbon-nanotube sensors. Small. 2009; 5:2528–2532. [PubMed: 19697305]
6. Lu W, Lieber CM. Nanoelectronics from the bottom-up. Nature Mater. 2007; 6:841–850. [PubMed: 17972939]
7. Grinvald A, Hildesheim R. VSDI: A new era in functional imaging of cortical dynamics. Nature Rev Neurosci. 2004; 5:874–885. [PubMed: 15496865]
8. Scanziani M, Häusser M. Electrophysiology in the age of light. Nature. 2009; 461:930–939. [PubMed: 19829373]
9. Purves, RD. Microelectrode methods for intracellular recording and ionophoresis. London: Academic Press; 1981.
10. Sakmann B, Neher E. Patch clamp techniques for studying ionic channels in excitable membranes. Ann. Rev. Physiol. 1984; 46:455–472. [PubMed: 6143532]
11. Molleman, A. Patch clamping: an introductory guide to patch clamp electrophysiology. England: Wiley, Chichester; 2003.
12. Wightman RM. Probing cellular chemistry in biological systems with microelectrodes. Science. 2006; 311:1570–1574. [PubMed: 16543451]
13. Ewing AG, Strein TG, Lau YY. Analytical chemistry in microenvironments: single nerve cells. Acc. Chem. Res. 1992; 25:440–447.
14. Schrlau MG, Dun NJ, Bau HH. Cell electrophysiology with carbon nanopipettes. ACS Nano. 2009; 3:563–568. [PubMed: 19309170]
15. Donoghue JP. Connecting cortex to machines: recent advances in brain interfaces. Nature Neurosci. 2002; 5:1085–1088. [PubMed: 12403992]
16. Leong M, Doris B, Kedzierski J, Rim K, Yang M. Silicon device scaling to the sub-10-nm regime. Science. 2004; 306:2057–2060. [PubMed: 15604400]
17. Ferrari M. Cancer nanotechnology: opportunities and challenges. Nature Rev. Cancer. 2005; 5:161–171. [PubMed: 15738981]
18. Tian BZ, Xie P, Kempa TJ, Bell DC, Lieber CM. Single-crystalline kinked semiconductor nanowire superstructures. Nature Nanotech. 2009; 4:824–829.
19. Materials and methods are available as supporting materials on Science Online.
20. Conde C, Cáceres A. Microtubule assembly, organization and dynamics in axons and dendrites. Nature Rev. Neurosci. 2009; 10:319–332. [PubMed: 19377501]
21. Leong TG, Randall CL, Benson BR, Bassik N, Stern GM, Gracias DH. Tetherless thermobiochemically actuated microgrippers. Proc. Natl. Acad. Sci. USA. 2009; 106:703–708. [PubMed: 19139411]
22. Misra N, Martinez JA, Huang S-CJ, Wang YM, Stroeve P, Grigoropoulos CP, Noy A. Bioelectronic silicon nanowire devices using functional membrane proteins. Proc. Natl. Acad. Sci. USA. 2009; 106:13780–13784. [PubMed: 19667177]
23. Zhou XJ, Moran-Mirabal JM, Craighead HG, McEuen PL. Supported lipid bilayer/carbon nanotube hybrids. Nature Nanotech. 2007; 2:185–190.
24. Chernomordik LV, Kozlov MM. Mechanics of membrane fusion. Nature Struct. Mol. Biol. 2008; 15:675–683. [PubMed: 18596814]
25. Claycomb WC, Lanson NA, Stallworth BS, Egeland DB, Delcarpio JB, Bahinski A, Izzo NJ. HL-1 cells: A cardiac muscle cell line that contracts and retains phenotypic characteristics of the adult cardiomyocytes. Proc. Natl. Acad. Sci. USA. 1998; 95:2979–2984. [PubMed: 9501201]
26. Almquist BD, Melosh NA. Fusion of biomimetic stealth probes into lipid bilayer cores. Proc. Natl. Acad. Sci. USA. 2010; 107:5815–5820. [PubMed: 20212151]
27. Bers DM. Cardiac excitation-contraction coupling. Nature. 2002; 415:198–205. [PubMed: 11805843]
28. Zipes, DP.; Jalife, J. Cardiac electrophysiology: from cell to bedside. ed. 2. Philadelphia, PA: Saunders; 2009.

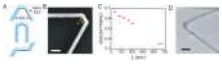

Fig. 1. Synthesis of kinked silicon nanowire probes

A, Schematics of 60° (top) and 0° (middle) multiply-kinked nanowires, and '*cis*' (top) and '*trans*' (bottom) configurations in nanowire structures. The blue and magenta regions designate source/drain (S/D) and nanoscale FET channel, respectively. **B**, SEM image of a doubly-kinked nanowire with '*cis*' configuration. *L* is the length of segment between two adjacent kinks. **C**, *cis*/(*cis* + *trans*) *vs. L* plot. **D**, Transmission electron microscopy image of an ultrathin 60° kinked nanowire. Scale bars, 200 nm in **B**, 50 nm in **D**.

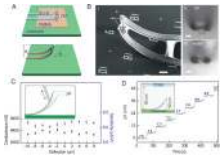

Fig. 2. 3D kinked nanowire probes

A, Schematics of device fabrication. Patterned PMMA and SU-8 micro-ribbons [see Materials and Methods (19)] serve as sacrificial layer and flexible device support, respectively. The dimensions of the lightly doped n-type silicon segment (white dots) are ca. $80 \times 80 \times 200$ nm^3. *H* and θ are tip height and orientation, respectively, and "S, D" designate the built-in source and drain connections to the nanoscale FET. **B**, SEM (**I**) and bright field optical microscopy (**II, III**) images of an as-made device. The yellow arrow and magenta star mark the nanoscale FET and SU-8, respectively. **II** and **III** are recorded in air and water, respectively. The scale bar is 5 μm. **C**, Device conductance and sensitivity as a function of deflection of the probe using a micropipette controlled with a micromanipulator. The measurements were carried out in PBS solution. Inset, experimental scheme. **D**, Change in potential vs. solution pH for a representative 3D nanowire probe. Inset, experimental scheme. For clarity, the 'point-like' FET elements are not labelled in schematics in **C** and **D**.

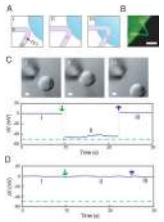

Fig. 3. Surface modification and cellular entry

A, Schematics of nanowire probe entrance into a cell. Purple, light purple, magenta and blue colors denote the phospholipid bilayers, heavily doped nanowire segments, active sensor segment and cytosol, respectively. **B**, False color fluorescence image of a lipids coated nanowire probe. DMPC was doped with 1 % NBD-dye labelled lipids and imaged through a 510/21 band pass filter. **C**, Differential interference contrast (DIC) microscopy images (upper panels) and electrical recording (lower panel) of an HL-1 cell and 60° kinked nanowire probe as the cell approaches (I), contacts and internalizes (II), and is retracted from (III) the nanoprobe. A pulled glass micropipette (inner tip diameter, ~ 5 μm) was used to manipulate and voltage-clamp the HL-1 cell. Dashed green line corresponds to the micropipette potential. Scale bars: 5 μm. **D**, Electrical recording with a 60° kinked nanowire probe without phospholipids surface modification. Green and blue arrows in **C** and **D** mark the beginnings of cell penetration and withdrawal, respectively.

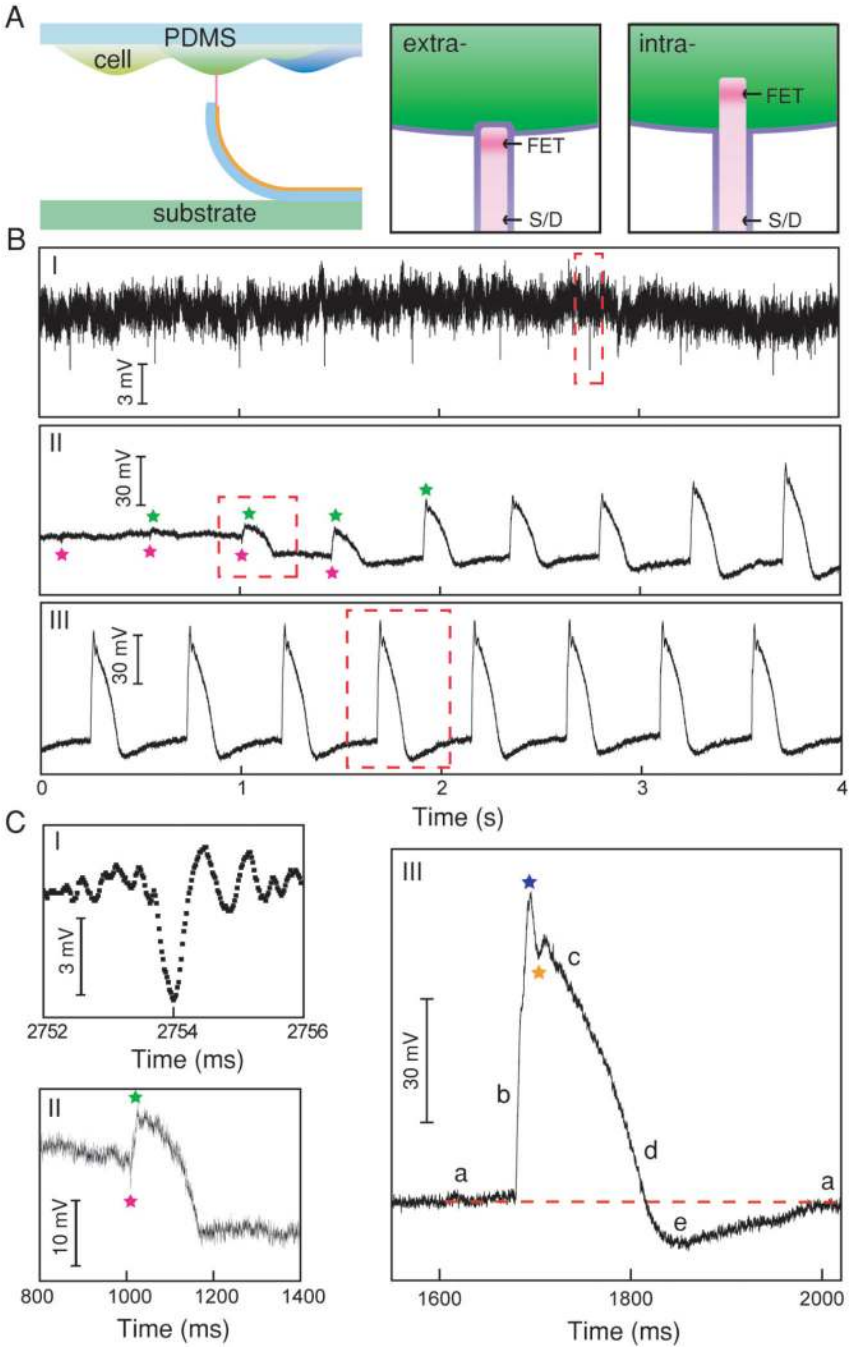

Fig. 4. Electrical recording from beating cardiomyocytes

A, Schematics of cellular recording from cardiomyocyte monolayer on PDMS (left panel), and highlight of extracellular and intracellular nanowire/cell interfaces (middle and right panels). The cell membrane and nanowire lipids coatings are marked as purple lines. **B**, Electrical recording from beating cardiomyocytes. I) extracellular recording. II) a transition from extracellular to intracellular recordings during cellular entrance and III) steady-state intracellular recording. Green and magenta stars mark the peak positions of intracellular and extracellular signal components, respectively. **C**, Zoom-in signals from the corresponding red-dashed square regions in (**B**). Blue and orange stars designate features associated possibly with inward sodium and outward potassium currents, respectively. **a-e** are five

characteristic phases of a cardiac intracellular potential as defined in text. The red-dashed line is the baseline corresponding to intracellular resting state. The cell culture, electronics and recording details are specified in Materials and Methods (19).